The Dynardo hydraulic fracturing simulator – coupled hydraulic-mechanical-proppant transport simulation of hydraulic stimulation in jointed rock

Johannes Will, Stefan Eckardt: Dynardo GmbH

1 Introduction

Substantial quantities of oil and gas are currently being produced from Unconventional Resources / Reservoirs. These reservoirs are usually characterized by high shale content and ultra-low matrix permeabilities. Most completions in Unconventional Reservoirs are hydraulically fracture stimulated in order to establish a more effective flow from the far-field reservoir and fracture network to the wellbore. The success of hydraulic fracture stimulation in horizontal wells has resulted in it being ranked as one of the major distinguishing technologies of the 21st Century. It has already realized its potential to dramatically change the oil and gas production landscape across the globe, and the impact will endure for decades to come.

For a given field development project, the derived economics is highly dependent on the effectiveness of the drilling and completion operation to establish effective and retained contact with the hydrocarbon resource. This paper introduces a suggested process to model, calibrate, and optimize the landing of the well and the optimization of the hydraulic fracture stimulation design for naturally fractured reservoirs.

The introduced workflow combines the commercial software packages ANSYS® [1] and multiPlas [2] within a 3D Hydraulic Fracturing Simulator [3] for the parametric Finite Element (FEM) Modeling and material modeling of naturally fractured sedimentary rocks. With the utility of optiSLang® [4], automated sensitivity studies of the uncertainty of reservoir, engineering, and operational parameters are performed and are evaluated relative to the resulting Stimulated Reservoir Volume (SRV) and Accessible Hydrocarbon Resource. Results from these studies are then used to optimize the well placements and completion designs.

Unlike most academic and commercial approaches, the introduced approach uses a homogenized continuum approach to model the 3D hydraulic fracturing in naturally fractured reservoirs. The principal motivation for using a continuum approach is the numerical efficiency necessary to run fully 3D coupled hydraulic/mechanical simulations of the hydraulic fracturing of multiple stages and multiple wells in naturally fractured sedimentary rocks. A fully 3D discrete fracture simulator respective of Mohr-Coulomb failure is quite numerically intensive. A discrete fracture model has not yet been developed using a fully 3D explicit fracture growth modeling system.

Hydraulic fracturing in shale reservoirs is mostly dominated by the anisotropic stress and strength conditions resulting from the initial patterns of planes of weakness, these usually being the natural joints and fractures of the source rock. To capture this impact on fracture mechanics, the three-dimensional modeling of anisotropic strength, stress, and conductivity of the matrix and of the fracture system is required. Simulation simplification to 2D or pseudo-3D geometric modeling will fail to capture the effects necessary to properly model the potentially most important effects which may drive the hydraulic fracturing process and the resulting production performance.

The homogenized continuum approach was initially developed and applied in the Civil Engineering field of Waterway and Dam Engineering to better determine the influence of water flow in naturally fractured dam foundations [5]. It was improved and generalized for the coupled hydraulic-mechanical simulation of naturally fractured rocks using commercial FEM codes [6]. These developments provide

the basis for the software tool “multiPlas” [2], which provides for the non-linear modeling of jointed rocks.

The introduced workflow is an integrated well placement and completion design optimization workflow. The toolkit integrates geomechanic descriptions, formation characterizations, flow dynamics, microseismic event catalogues, hydraulic fracturing monitoring data, well completion and operational parameters in a modeling environment with optimization capability. It is built upon a 3D geological model with multi-disciplinary inputs including formation properties, in-situ stresses, natural fracture descriptions, and well and completion parameters (i.e., well orientation, landing interval, fluid rate and volume, perforation spacing, and stage spacing). Upon calibrating with the hydraulic fracturing field observations, the introduced workflow optimized well completion design, and guidance on data acquisition and diagnostic needs to achieve EUR performance at optimized costs.

1.1 Background on Dynardo’s Hydraulic Fracturing Modeling Approach

The inherent anisotropies of unconventional reservoirs result from layering, deformation history, strength and stress variability, and the non-uniform conductivity of the fractured rock mass. Because of these complexities, hydraulic fracturing should be simulated in a fully three-dimensional coupled hydro-mechanical model. Most shale hydrocarbon resources are essentially jointed even before hydraulic fracturing takes place. These planes of weakness include the bedding plane and usually two or three additional sets of natural planes of weakness.

Most commercial hydraulic fracture simulators model hydraulic fracturing using 1D, 2D, or pseudo 3D geometric approaches. In many cases, these simplifications prevent the simulators from adequately modeling the complex hydraulic fracturing mechanisms that are present. This may dramatically oversimplify the simulated fracture geometry, and may fail to identify the opportunities for economic production improvement in all but the most trivial of shale resource settings [7].

For a fully 3D modeling approach, achieving an effective numerical discretization capable of representing multiple stages and multiple wells in a complex reservoir setting is necessary. A discrete modeling approach of natural fractures or a homogenized modeling approach of fractures can be developed. However, the discrete modeling of a network of joints resulting from the hydraulic fracturing of the rock mass is currently computationally “extraordinarily expensive” to the point of impracticality for wellbore-scale models. Such models include discrete element and particle approaches (DEM, Particle codes) or discrete fracture modeling in continuum mechanics approaches (XFEM, cohesive zone elements). Currently, there are no commercial simulation solutions available for the wellbore-scale fully 3D hydraulic fracturing simulation of multiple stages and multiple wells using discrete joint modeling. Although a majority of research groups are following discrete fracture modeling approaches, a fully 3D discrete solution appears elusive at the needed wellbore-scale.

The modeling of coupled hydro-mechanical problems in rock mechanics using a homogenized continuum strategy was successfully implemented for science and industrial applications by Wittke [5] and others in the 1980s and 1990s. The weak point of the numerical implementation at that time was the inability of consistent integration of multi-surface plasticity, which is a result of dealing with multiple yield criteria at the material point level in the homogenized continuum representing intact rock (matrix) and multiple joint sets. To overcome the problem, Wittke introduced a pseudo-viscous numerical procedure which depended on pseudo-parameters which had a seemingly unreasonable influence on the results. Using a homogenized modeling approach for jointed rock in implicit integration algorithms resulted in convergence difficulties. Science groups moved to trial explicit time

integration procedures using discrete modeling techniques or particle based models. Here convergence problems are minimal. However, because of the stability requirements of explicit time integration schemes, these approaches became computationally “extraordinarily” time consuming when modeling transient 3D wellbore scale problems.

After attempting discrete joint modeling and explicit time integration methods for several years, researchers at the Bauhaus University in the late 90’s returned to a homogenized continuum approach, and developed a solution for the problem of consistent integration of multi-surface plasticity using implicit time integration [6]. As a result, hydraulic fracturing can now be efficiently modeled by using implicit finite element formulations, incorporating real world fully 3D reservoir conditions including all relevant anisotropies and thermo-hydro-mechanical coupling [8].

1.2 Every Hydraulic Fracturing Simulator Needs to be Calibrated for Typical Reservoir Conditions

A practical 3D Hydraulic Fracturing Simulator that could simulate multiple stages in multiple wells with reasonable numerical effort was now available. The challenge was then to properly characterize the geomechanical (stress, strengths, moduli, cohesion, friction angle, YM, PR, etc.) and the hydraulic (pressure, saturations, compressibility, permeability, etc.) setting of the resource. It is a formidable task to accurately measure the total state of the reservoir and bounding layers. However, in order to model realistic fracture height growths, all relevant potential fracture barriers need to be modeled and parameterized. Significant fracture barriers may occur due to layered contrast in deformation, stress, and strength characteristics. Similarly, faults and previously created hydraulic fractures may act as preferred mechanisms for fracture growth. These are generally to be expected when horizontal well fracture stimulations are closely staged.

After constructing a layered reservoir and bounding rock model inclusive of the potential fracture barriers, the calibration of large amounts of uncertain rock parameters to the best available measurements was necessary. A parameter identification problem exists simply because of the large number (>100) of model parameters, and they may have a considerable associated uncertainly. During the calibration phase, the workflow applies optiSlang [4], a commercial tool box for variation space management and optimization analysis. The process involves running a set of calibration models respective of the variation space of the model. With optiSLang, all parameters in a parametric hydraulic fracturing model can be identified and updated efficiently for successive model runs, which are then initialized and executed in an automated process. A large number of calibration sensitivity design runs can be executed in a comparatively short period of time.

The calibration phase ideally requires quality data measurements. This includes the pressure measurements that are used to derive ISIP/DFIT (Instantaneous Shut-In Pressure, Dynamic Fracture Intensity Test) conditions as well as the projected bottom-hole pressure history. The representative microseismic event catalog is also used in the calibration phase. Uncertainty analysis is integrated in the calibration process to better identify the most influential parameters controlling fracture geometry. This calibration process also provides the potential to focus additional data gathering to those parameters that significantly affect the simulation results.

Once a calibrated model is developed that is respecting of the resource data as well as the microseismic event data, the simulator can then be used in a forecast mode to better optimize the well landing depth and the completion design.

1.3 What is the Right Value to be Optimized?

After having a 3D Hydraulic Fracturing Simulator that is well calibrated to the reservoir, the next question is “What are the right quantities to optimize?” Conventionally, Stimulated Rock Volume (SRV) is used to quantify the effectiveness of the fracture stimulation. SRV variation is clearly dominated by fluid volume variation: more frac fluid simply creates more fractures and more frac volume. The simulation results can be used to fully quantify which reservoir layers are being fractured, how much frac height and frac length is produced, which fractures accepts proppant based on apertures, and how the created fracture network might effectively drain the reservoir.

First, only created fractures that are acceptant of proppant with sustained connectivity to at least one perforation cluster or flow port are credited with production potential. The related proppant-accepting volume is referred to as **Valuable SRV** (VSRV). Second, the **drainage volume** over the productive life of the well is calculated based on the VSRV with consideration for an average drainage radius. By integration of the pore and hydrocarbon content in the reservoir layers over the drainage volume, the **Accessible Hydrocarbon Initially In Place (AHCIIP)** can be calculated. This represents the producible hydrocarbons connected to the wellbore. By applying a representative recovery factor, the estimated hydrocarbon production expected over the lifetime of the well is calculated. The economic maximization of AHCIIP is usually the optimization goal.

A very important verification of the forecast quality of the calibrated reservoir model is the comparison of the estimated hydrocarbon production from the hydraulic fracturing simulator to Estimated Ultimate Recovery (EUR) of the calibration well and neighboring wells.

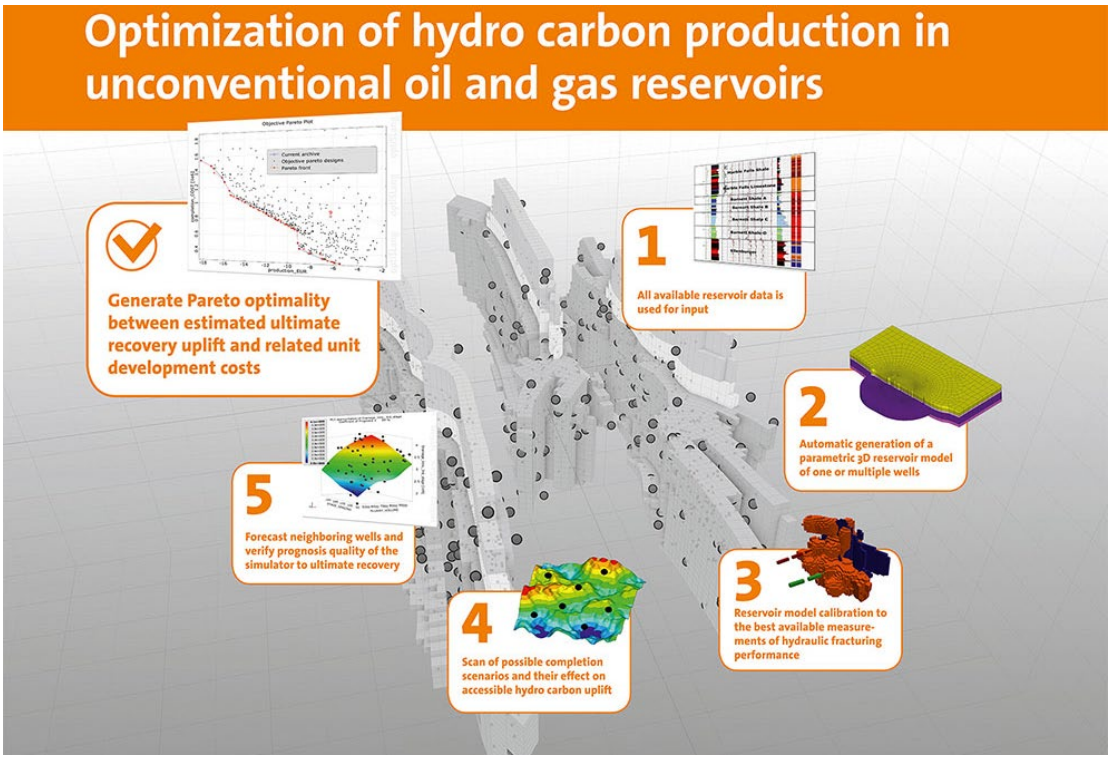

Fig. 1-1 worklow for optimization of hydrocarbon production in unconventional oil and gas reservoir

During the optimization procedure, the major completion parameters such as well orientation, landing depth, stage design, well spacing, and fluid volume will generally be the most influential parameters. The optimization process is usually a compromise between increasing EUR potential subject to

reducing completion costs. This optimization is represented by a classic Pareto Frontier. Using optiSLang, the Pareto Frontier represents the design limits where any production improvement cannot be introduced anymore without increasing the completion costs. The Pareto Frontier is the final result of the workflow. It is used for rationalizing the decision between maximizing AHCIIP and minimizing the related completion costs.

2 The Dynardo Hydraulic Fracturing Simulator

The Hydraulic Fracturing Simulator [3] combines three commercial software packages: ANSYS® [1], the Dynardo hydraulic fracture simulator [..] on top of ANSYS including the material model library multiPlas [2] and optiSLang® [4]. ANSYS is used for the development of parametric reservoir finite element models and as solver. The coupled hydraulic-mechanical-proppant transport analysis is performed with the hydraulic fracturing simulator. The module, multiPlas, is an ANSYS extension for non-linear material modeling of geomaterials. These material models extend the ANSYS functionality to the non-linear mechanical analysis of naturally fractured rocks. Within the context of the hydraulic fracturing simulator, Dynardo provides user defined finite elements for the hydraulic and the proppant transport part as well as user defined APDL-functions for the efficient coupling of the sub-models. The third software product, optiSLang, is used to efficiently calibrate the model and to perform sensitivity analyses in consideration of the uncertainties in the reservoir model and operational conditions. Finally, Dynardo currently develops Tamino – a post-processing tool for the hydraulic fracturing simulations. In the future, this tool will be also used for the pre-processing of the reservoirs.

2.1 Homogenized continuum approach

In order to reach a sufficient forecast quality in the simulation of hydraulic fracturing, the most important phenomena that needs to be represented by the model is the three-dimensional anisotropic strength and conductivity distribution in naturally fractured sedimentary rocks. In the case of unconventional gas and oil shale, the rock is classified as jointed rock having isotropic “intact” rock strength and multiple sets of planes of weakness. For the purpose of this document, these planes of weakness are called “joint sets”. Obviously the sedimentary rock has a bedding plane (see Fig. 2-1, label “joint set 3”). There are often two additional sets of strength anisotropies (see Fig. 2-1, labels “joint set 1, joint set 2”). In some reservoir layers these joint sets are either open or cemented/healed.

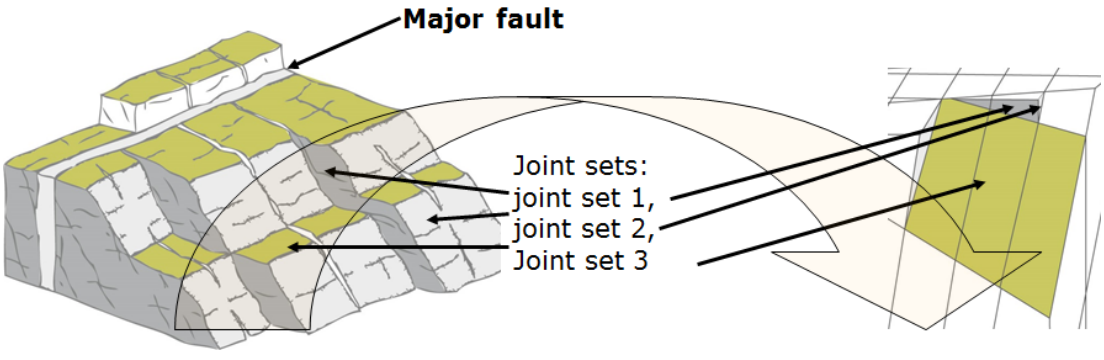

Fig. 2-1 Jointed rock characterization and translation to homogenzied continuum approach

In some instances, these joint sets can be identified on various open hole logs or cores. In other instances, these joint sets are closed and the identification of the joint sets in open hole logs or cores might be difficult.

The fracture simulator applies the continuum approach which is based on the concept of homogenization. In contrast to discrete models, the joint sets are not explicitly modeled as geometry boundaries. The influence of the joint sets is explicitly taken into account within the anisotropic strength model of jointed rock which results in an anisotropic conductivity development in the event of the rock failure represented by the element. Essentially, a joint set dilates opens, and the associated conductivity increases due to either an oriented tensile or an oriented shear failure. At the conclusion of the frac job, the net pressure decline may result in the joint set aperture reducing, resulting in a reduction of the associated conductivity. Both of these effects are taken into account in the simulator.

In the simulation, the tensile and shear failure modes of intact rock and of the individual joint sets are consistently treated within the framework of multi-surface plasticity [9]. The multi-surface strength criterion is evaluated at every discretization point in space. If the stress state violates the multi-surface yield criterion, then plastic strains develop and strength degradation occurs. By introducing "mean effective" activated joint set frequencies that can be defined for every joint set and for every individual layer, the homogenized joint openings and the corresponding joint conductivities can be calculated based on the plastic strains. The individual values can be evaluated and visualized in the post-processing step. The initial natural frequency of the planes of weakness and the mean effective activated frequency of stimulated joints will usually vary. As a result, determining the activated average frequency of joints is an important undertaking in the calibration process.

The homogenization approach can and should be coupled with discrete anisotropies such as major faults if the dimensions of the discrete anisotropies are large compared to the overall modelled 3D geometry or if discrete effects at major faults are of interest. The fault is modelled as discrete 3D geometry feature, and an oriented joint set is used to define the shear and tensile strength criteria of the fault.

2.2 Parametric Reservoir Modeling

The simulation of hydraulic fracturing requires the calibration of important but somewhat uncertain parameters. The reservoir system, inclusive of the wellbores and the frac stages, should be parametrically modeled in order to allow for an efficient calibration procedure. The entire process of model generation (pre-processing), model solution, and model post-processing should ideally be an automated process. The hydraulic fracturing simulator offers a predefined parametric representation of the following inputs:

1/ **Reservoir geometry:** number, depth and thickness of all rock units (layers)

2/ **Material properties of all rock layers:** linear and nonlinear mechanical material properties including definition of up to four joint sets, hydraulic material properties

3/ **Initial stress field:** piece-wise linear distribution (linear inside one layer, but jumps at the boundary between two layers) of total vertical stress, minimum horizontal effective stress (k0-values) and maximum horizontal effective stress, direction of minimum horizontal stress

4/ **Initial pore pressure field:** piece-wise linear distribution of pore pressure (linear inside one layer, but jumps at the boundary between two layers)

5/ **Coupling parameters:** average activated joint set distance, joint set roughness coefficient, stress dependency of joint conductivity

6/ **Well/Stage design parameters:** number of wells/stages, stage positions and orientations, number of perforation clusters per stage, distance between perforations, distance between stages, well/stage depths, horizontal well orientation, well dip

7/ **Well treatment:** slurry rate, slurry volume or bottom hole pressure as a function over time, fluid viscosity, perforation conductivities

8/ **Proppant job parameters:** number of proppant classes, average proppant diameter, apparent proppant density, proppant inflow as function of time, critical proppant concentration

9/ **Finite element mesh:** definition of model boundaries, definition of volumes with different element size (e.g. fine mesh at perforations and coarse mesh at the model boundary), element size, type of mesh, type of coupling, perforation size

10/ **Simulation parameters:** time stepping, post-processing

The parametric modeling approach is derived from the ANSYS internal programming language APDL.

Most of the parameters are separately defined for each distinctive rock layer and for each joint set. Several hundred parameters are generally required for a model run. As part of the parameter definition/selection processing; the automatic generation of the finite element model, the calculation of in-situ reservoir conditions, and the well design and the operational conditions are all tested for consistency before a unique model execution begins. On occasion, a parameter selection is made for a specific model run that results in an unrealistic (unstable) initial condition. When this occurs, these unstable models are identified and their run time execution is terminated.

2.3 Coupled Hydraulic-Mechanical-Proppant transport Analysis

Hydraulic fracturing is first of all a coupled hydraulic-mechanical problem. In the hydraulic module, the pressure increases in the fracture initialization location due to the pumping of fluid and low initial rock permeability. Within the homogenized continuum approach, pressure is treated as “pore pressure” representing the pressure in the fracture network. In the mechanical part the increase of pressure modifies the effective stresses acting on the rock. If the pressure is large enough, the jointed rock fails and fractures start to open. As a result, the rock permeability increases, which directly influences the pressure distribution in the hydraulic module. If proppant is additionally pumped, then the hydraulic fracturing process becomes a coupled hydraulic-mechanical-proppant transport problem. On the one hand, the transport and placement of proppant depends on the fracture geometry (mechanical module) as well as the fluid flow (hydraulic module). On the other hand, proppant prevents closure of a fracture and reduces the permeability of the fracture. In the simulation of hydraulic fracturing, these primary coupling effects need to be resolved. Fig. 2-2 shows a flowchart of a coupled hydraulic-mechanical-proppant transport analysis with the Dynardo hydraulic fracturing simulator.

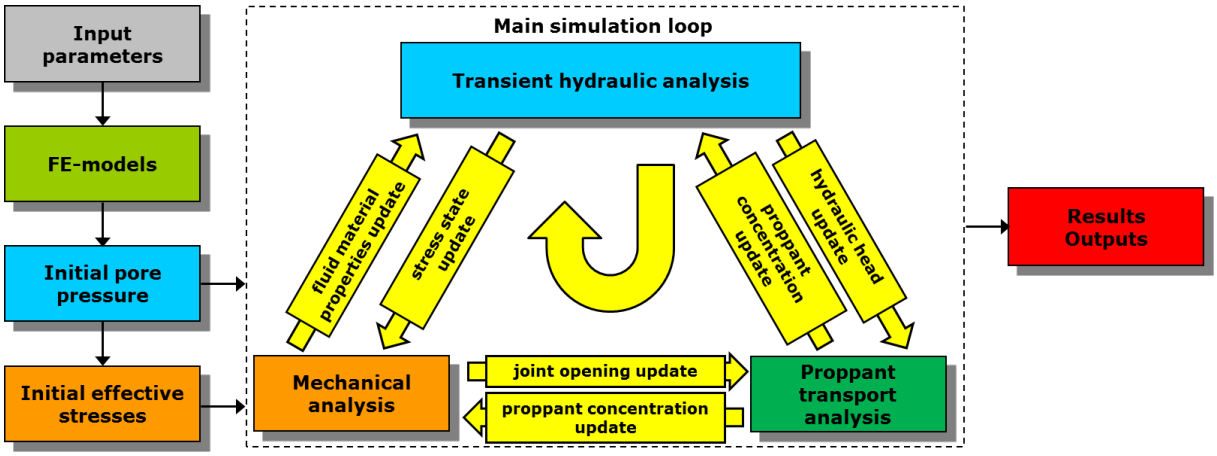

Fig. 2-2 Schematics of 3D coupled hydraulic-mechanical-proppant transport simulation

The automatic simulation procedure starts with the setup of the reservoir geometry based on a set of input parameters representing the layering, the well, and the stage design. Based on these parameters the finite element models are generated and the in-situ conditions are applied. In the hydraulic model, the pore-pressure field is initialized with the initial reservoir pore pressure conditions. The mechanical model is initialized with the initial effective stress distribution. A non-linear mechanical analysis is performed to ensure consistency between the mechanical parameters and the initial stress field. The initial conditions should not result in plastic strains in the model. Assuming zero initial proppant concentrations, no special initialization procedure is required for the proppant sub-model.

After model initialization, the actual simulation cycle for hydraulic fracturing starts. In each cycle, the hydraulic, proppant transport and the mechanical sub-model are independently solved. The coupling between the models is realized by an update of material parameters and loading conditions in the corresponding sub-models. The following couplings are applied:

1/ **Stress state update (hydraulic-mechanical coupling):** based on the pore-pressure distribution in the hydraulic model, flow forces are applied in the mechanical analysis.

2/ **Fluid material properties update (mechanical/proppant transport-hydraulic coupling):** based on the plastic strain and the stress distribution in the mechanical model together with the proppant concentration obtained from the proppant transport model, the conductivities are updated in the hydraulic model. Because of the anisotropic failure of the joint sets, an anisotropic conductivity tensor is obtained.

3/ **Proppant concentration update (proppant transport-mechanical/hydraulic coupling):** based on the proppant concentration the residual joint opening (closure function) in the mechanical model is updated and the influence of proppant on the hydraulic joint conductivity is considered in the fluid material properties updated (see point 2/).

4/ **Joint opening update (mechanical-proppant transport update):** based on the plastic strain and the stress distribution in the mechanical model, the fractured elements and the corresponding joint parameters - joint opening, joint conductivity, joint orientation - are updated in the proppant transport model.

5/ **Hydraulic head update (hydraulic-proppant transport update):** the hydraulic head distribution is transferred to the fractured elements in the proppant transport model. Based on the hydraulic heads the joint slurry velocities are calculated.

The coupling is performed in an explicit way. Consequently, one iteration cycle is performed for every time step. The time step needs to adequately represent the progress of the fracture growth. The cycle starts with the transient hydraulic analysis. The pore-pressure field is updated and the corresponding flow forces are calculated and applied to the mechanical model. Furthermore, the hydraulic heads are transferred to the proppant transport model. The next step is the transient transport simulation. The updated proppant concentrations are exported and transferred to the mechanical model. The final step is the nonlinear mechanical analysis which results in a new stress and plastic strain distribution. The resultant update of the hydraulic conductivities in the hydraulic model and the joint parameters in the proppant transport model is applied in the subsequent time-step.

2.4 Non-Linear Mechanical Analysis

In the mechanical sub-model, a nonlinear static finite element analysis, cf. [10], is performed. The nonlinearities are caused by failure of the material. In ANSYS, the nonlinear constitutive behavior of jointed rock is described with the external library multiPlas [2]. By using the ANSYS “usermat” API for user-defined material models, multiPlas provides nonlinear material models for typical materials in geomechanical and civil engineering studies.

The mechanical analysis of jointed rock incorporates the concept of effective stresses. This is the stress which directly acts on the rock and which results in a deformation of the rock. The effective stress tensor $\boldsymbol{\sigma_{eff}}$ is defined as:

$$\boldsymbol{\sigma_{eff}} = \boldsymbol{\sigma_{tot}} - p\boldsymbol{I} \qquad (2\text{-}1)$$

where $\boldsymbol{\sigma_{tot}}$ is the total stress tensor, p is the pore-pressure and $\boldsymbol{I}$ is the second order identity tensor.

The homogenized continuum approach is applied to describe the deformation behavior of jointed rock. Consequently, the stress-strain relationship does not describe the deformation behavior of the individual constituents, intact rock and joint sets, but the overall response of the homogenized jointed rock mass. The corresponding linear-elastic stress strain relationship can be written as:

$$\boldsymbol{\sigma_{eff}} = \boldsymbol{D} : \boldsymbol{\varepsilon} \qquad (2\text{-}2)$$

where $\boldsymbol{D}$ is the generally orthotropic linear elastic material tensor of the homogenized rock mass and $\boldsymbol{\varepsilon}$ is the strain tensor.

In multiPlas, the description of the nonlinear behavior of jointed rock is based on the concept of rate-independent plasticity, cf. [9] [11]. It is assumed that the total strain $\boldsymbol{\varepsilon^{tot}}$ can be decomposed into an elastic part $\boldsymbol{\varepsilon^{el}}$ and a plastic part $\boldsymbol{\varepsilon^{pl}}$:

$$\boldsymbol{\varepsilon^{tot}} = \boldsymbol{\varepsilon^{el}} + \boldsymbol{\varepsilon^{pl}}. \qquad (2\text{-}3)$$

The stresses are related to the elastic strains by the linear elastic material matrix. Consequently, Eq. (2-2) can be rewritten as:

$$\boldsymbol{\sigma_{eff}} = \boldsymbol{D} : \boldsymbol{\varepsilon^{el}}. \qquad (2\text{-}4)$$

The plastic strains develop if a certain strength criterion, conventionally referred to as the yield condition, is violated. In this context, the boundary of the admissible stress space (elastic domain) is called yield surface.

The strength of the homogenized jointed rock is defined by the strength of the individual constituents. As a result, the overall strength criterion is not a smooth surface, but is composed of multiple yield surfaces. Each yield surface represents a specific failure mode of one of the constituents.

In the multiPlas material model for jointed rock, isotropic strength is assumed for intact rock. Two fundamental failure modes are considered. Tensile failure of intact rock is represented by the Rankine yield surface. The corresponding yield condition can be written as:

$$F_{RK,I} = \sigma_1 - f_{t,I} \leq 0, \qquad (2\text{-}5)$$

where σ_1 is the maximum effective principal stress (tensile stresses are positive) and $f_{t,I}$ is the uniaxial tensile strength. Shear failure of intact rock is described by the Mohr-Coulomb yield condition, which reads:

$$F_{MC,I} = \frac{\sigma_1 - \sigma_3}{2} + \frac{\sigma_1 + \sigma_3}{2}\sin\varphi_I - c_I\cos\varphi_I \leq 0, \qquad (2\text{-}6)$$

where φ_I is the intact rock friction angle, c_I the cohesion, σ_1 is the maximum effective principal stress, and σ_3 is the minimum effective principal stress.

The multiPlas material model currently allows the definition of up to four joint sets. In contrast to intact rock, the joint strength criteria are anisotropic. The strength criteria of a particular joint set

depend on the joint orientation, which is described by the strike angle α and the dip direction β. The corresponding yield surfaces are defined in terms of the normal joint stress $\sigma_{N,J}$ and the in-plane shear stress τ_J. Both stress components are obtained by rotating the global stress tensor into the local joint coordinate system. Similar to intact rock, two failure modes are taken into account for every joint set. The tension cut-off yield surface represents tensile failure normal to the joint. The corresponding yield condition reads:

$$F_{T,J} = \sigma_N - f_{t,J} \leq 0, \qquad (2\text{-}7)$$

where $f_{t,J}$ is the tensile strength of the joint set. Joint shear failure is described by the Mohr-Coulomb yield surface:

$$F_{MC,J} = \tau_J + \sigma_N \tan\varphi_J - c_J \leq 0, \qquad (2\text{-}8)$$

where φ_J is the joint friction angle and c_J is the joint cohesion.

The individual yield surfaces of the multiPlas jointed rock material model are visualized in Fig. 2-3. If in the simulation a strength criterion becomes active, the corresponding strength parameters are reduced to residual values. Dilatancy effects are taken into account for shear failure by incorporating non-associated flow rules. The corresponding plastic potentials are obtained from the Mohr-Coulomb conditions by replacing the friction angle with the dilatancy angle in Eqs. (2-6) and (2-8).

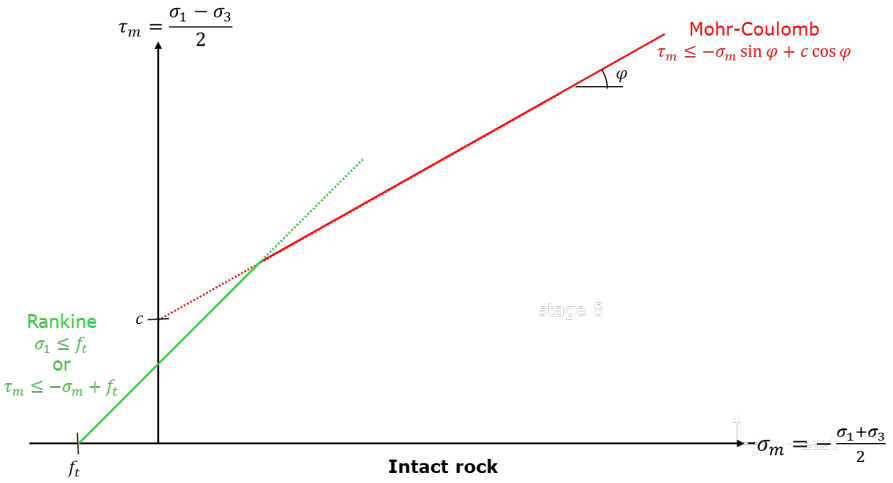

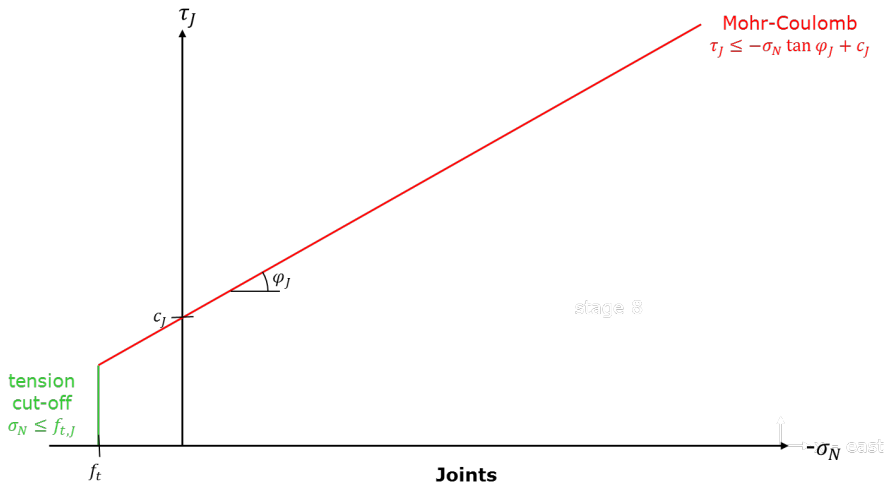

Fig. 2-3 Jointed rock yield surfaces of intact rock and joint sets in multiPlas

2.4.1 Consistent Numerical Treatment of Multiple Strength Conditions

The non-linear behavior of jointed rock is described by a set of different strength conditions. As a result, the boundary of the admissible stress space becomes non-smooth which requires a special numerical treatment. In multiPlas, the multi-surface plasticity approach, introduced by [9], is implemented which allows for an efficient and consistent treatment of multiple yield conditions.

In the multi-surface plasticity approach, the plastic strain increment is defined by a modified flow rule which can be written as:

$$\boldsymbol{\Delta\varepsilon^{pl}} = \sum_{\alpha=1}^{n_{YC}} \Delta\lambda^{\alpha}\boldsymbol{g^{\alpha}} \qquad (2\text{-}9)$$

where n_{YC} is the number of yield conditions, $\Delta\lambda^{\alpha}$ is the plastic multiplier and $\boldsymbol{g^{\alpha}}$ is the direction of plastic flow of yield condition α. A stress state is admissible if all yield conditions are satisfied. If the stress state is on a yield surface, then plastic strains develop for that yield surface. Because the flow rule defines an oriented direction of plastic flow, the corresponding plastic multiplier must be positive. Any stress state must satisfy these conditions, which are known as Kuhn-Tucker or loading/unloading conditions, for each yield criterion:

$$F_{\alpha} \leq 0 \qquad F_{\alpha}\Delta\lambda^{\alpha} = 0 \qquad \Delta\lambda^{\alpha} \geq 0 \qquad \alpha = 1 \ldots n_{YC}. \qquad (2\text{-}10)$$

Consequently, in a plastic step, the stress state might be located on more than one yield surface. This is illustrated in Fig. 2-4 for a two surface model. In order to handle the singularity at the intersection between both yield surfaces, the stress state must satisfy both conditions. As a result, the direction of plastic strain is defined as a combination of the individual directions.

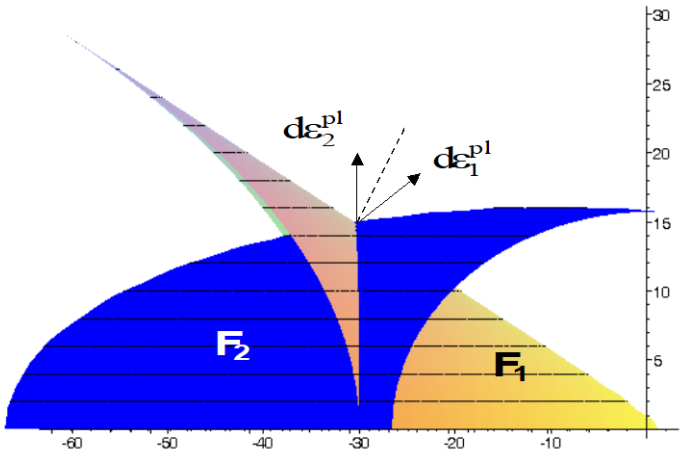

Fig. 2-4 Intersection between the two flow criteria F1 and F2

In the numerical implementation, the stress-calculation is performed in two steps. In the first step, a trial stress state is calculated assuming that the plastic strain obtained in the previous step does not change. The yield conditions are evaluated for this trial stress state. A set of active yield surfaces is defined by all yield conditions which are violated by the trial stress state. If the set of active yield surfaces is empty, the trial stress state is admissible. Otherwise, the trial stress needs to be returned to all active yield surfaces. In this second step, the standard return mapping algorithms, i.e., cutting plane or closest point projection, are applied. In contrast to the classical single-surface plasticity, the return mapping algorithm must simultaneously handle multiple yield surfaces which results in a system of generally nonlinear equations. An additional activity condition is introduced. A yield condition is

removed from the set of active yield surfaces if the corresponding plastic multiplier becomes negative during the iteration.

2.5 Hydraulic Analysis

In the hydraulic step, a transient analysis is performed. In order to cover gravity effects, the governing equations are not expressed in terms of the pore-pressure, but rather in terms of the hydraulic head. The hydraulic head h of a fluid is defined as the combination of the pressure head and the elevation head:

$$h = \frac{p}{\rho g} + z, \qquad (2\text{-}11)$$

where p is the pore-pressure, ρ is the fluid density, g is the standard gravity and z is the elevation.

The analysis is based on the groundwater flow equation:

$$S_s \frac{\partial h}{\partial t} = -\nabla \boldsymbol{q} + R \qquad (2\text{-}12)$$

where S_s is the specific storage, R is a general source and sink term, and $\boldsymbol{q}$ is the flux vector. The specific storativity is one of the most important hydraulic parameters that needs to be calibrated for the reservoir. The storativity represents the amount of stored energy in open joints, and is related to the energy losses due to friction or of leakage during the hydraulic fracturing process.

Similar to the mechanical model, the continuum theory is applied in the hydraulic model. As a result the flux vector can be related to the hydraulic head by Darcy's law:

$$\boldsymbol{q} = -\boldsymbol{K}\,\nabla h \qquad (2\text{-}13)$$

where $\boldsymbol{K}$ is the conductivity matrix of the jointed rock.

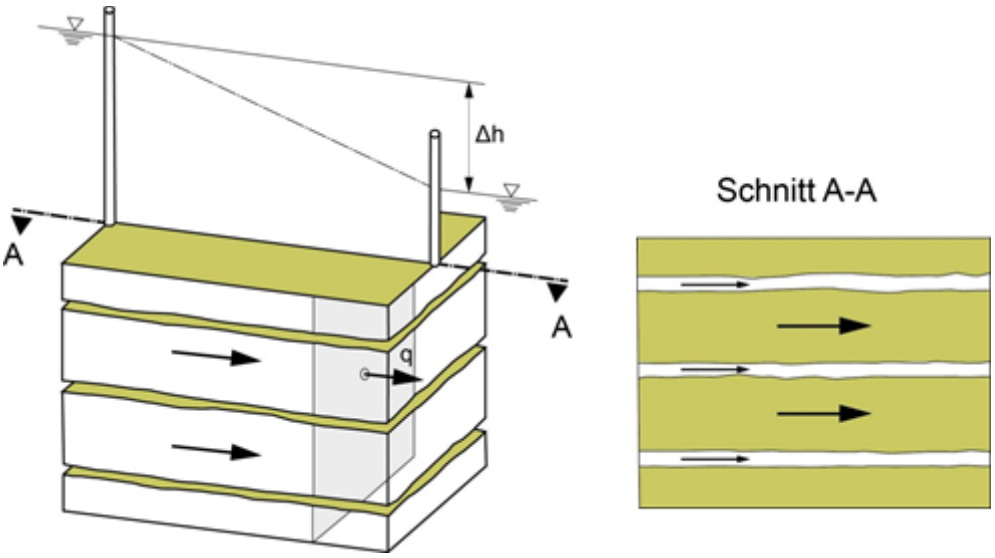

Fig. 2-5 Darcy flow equation in homogenized continuum mechanics

As shown in Fig. 2-5, the Darcy equation describes the flow through the homogenized jointed rock. The hydraulic conductivity matrix $\boldsymbol{K}$ represents the overall conductivity of the rock including all joint sets. The homogenized conductivity is obtained by superimposing the contributions of the individual constituents:

$$\boldsymbol{K} = \boldsymbol{K_I} + \sum_{j=1}^{n_{JS}} \boldsymbol{K_J^{(j)}} \qquad (2\text{-}14)$$

where $\boldsymbol{K_I}$ is the hydraulic conductivity of intact rock, n_{JS} is the number of joint sets, and $\boldsymbol{K_J^{(j)}}$ is the hydraulic conductivity of joint set j.

In the simulator, the intact rock conductivity represents the initial rock conductivity. By assuming a transversely isotropic behavior, the intact rock conductivity matrix is given by:

$$\boldsymbol{K_I} = \frac{\rho\, g}{\mu}\begin{bmatrix} k_{ini,h} & 0 & 0 \\ 0 & k_{ini,h} & 0 \\ 0 & 0 & k_{ini,v} \end{bmatrix} \qquad (2\text{-}15)$$

where ρ is the fluid density, g is the standard gravity, μ is the dynamic fluid viscosity, $k_{ini,h}$ is the initial horizontal rock permeability, and $k_{ini,v}$ is the initial vertical rock permeability. It is to be noted, that failure of intact rock does not change the initial rock conductivity matrix. As shown in section 2.7.3, intact rock failure is handled by introducing additional joint sets.

A joint set allows flow in the joint plane, but not perpendicular to the joints. As a result, the joint conductivity matrix depends on the joint orientation. In the local joint coordinate system (z axis normal to the joint set), this matrix reads:

$$\boldsymbol{K_J'} = \frac{\rho\, g}{\mu} k_J \begin{bmatrix} 1 & 0 & 0 \\ 0 & 1 & 0 \\ 0 & 0 & 0 \end{bmatrix} \qquad (2\text{-}16)$$

where k_J is the in-plane joint permeability. In the initial state the joint permeability is zero. If a joint set fails, the joint opens up and the joint permeability increases. This relationship is described in detail in section 2.7. The global joint conductivity matrix is obtained by rotation of the local matrix:

$$\boldsymbol{K_J} = \boldsymbol{R}^T \boldsymbol{K_J'} \boldsymbol{R}, \qquad (2\text{-}17)$$

where $\boldsymbol{R}$ is a matrix describing the rotation from the global into the local joint coordinate system. Because of the anisotropic nature of the joint conductivity matrix, the homogenized conductivity matrix $\boldsymbol{K}$ becomes anisotropic during the simulation.

By substituting Eq. (2-13) into Eq. (2-12) the transient seepage equation is obtained:

$$S_s \frac{\partial h}{\partial t} = -\nabla(\boldsymbol{K}\,\nabla h) + R \qquad (2\text{-}18)$$

This equation is solved by using finite element techniques. Equation (2-18) is analogous to the heat equation in heat transfer problems. ANSYS heat transfer elements seemingly could solve the problem. However, because of the anisotropic hydraulic conductivity matrix, Dynardo implemented a new hydraulic element that more effectively manages the anisotropy. The implementation is based on the USER100 interface of ANSYS.

2.5.1 Well Treatment and Pipe Modeling

In the hydraulic model, the reservoir including the perforations is modelled by solid elements. In this context the solid perforation elements are modeled with a high conductivity perpendicular to the well and initial rock conductivity in well direction. Additional 1-D pipe elements are introduced to connect the perforations of one stage to the volume elements. These pipe elements are automatically created during the model generation process. Fig. 2-6 shows the pipe definition in the model. The red line represents the well bore which connects the perforations of a particular stage. The hydraulic properties

of the well bore are defined by the pipe diameter and the pipe conductivity. In general a large conductivity value is applied for the well bore. The green lines are the equivalent perforation pipes/tunnels that connect the well bore with the center of the reservoir volume elements. The perforation pipes are introduced to model a pressure drop between the well and the end of perforation. The hydraulic conductivity of the perforation pipes are defined in terms of a prescribed pressure drop ΔP:

$$K_{perf} = \frac{4\,\rho g\,L}{\pi\, d_{Perf}^2\,\Delta P}\frac{Q_{Ref}}{n_{Perf}} \qquad (2\text{-}19)$$

where L is the pipe length, d_{Perf} is the pipe diameter, Q_{Ref} is the reference slurry rate, and n_{Perf} is the number of perforations. It is to be noted, that Equation (2-19) assumes equal distribution of the slurry to the perforations. In the simulation as well as in the real world, the distribution of slurry to the perforations depends on the generated fractures and the resulting permeability distribution. If in one stage a perforation is connected to a higher permeable fracture than the other perforations, then more slurry is pumped through this particular perforation and the pressure drop increases in that perforation. Consequently, the pressure drop in a perforation might deviate from the prescribed pressure drop. Additionally, the pressure drop might change over time, even if a constant slurry rate is applied to the stage.

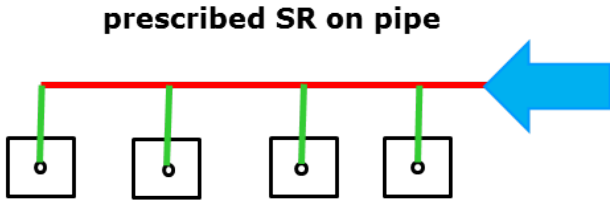

Fig. 2-6 Slurry Rate boundary condition

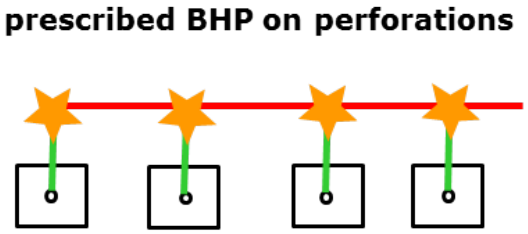

Fig. 2-7 Bottom Hole pressure boundary condition

In the simulator, the loading conditions are applied either to the well pipe or to the perforation pipe. Two types of loading conditions are supported.

An inflow condition is defined in terms of a prescribed slurry rate (SR) or a prescribed slurry volume (SV). By applying the slurry inflow to the well pipe, as shown in Fig. 2-6, the slurry in the perforation (the outflow from perforation to the reservoir) is defined by the conductivity buildup in the rock connected to the perforation.

Alternatively, a pressure condition can be applied to define bottom-hole pressure (BHP) conditions. During the model calibration, pressure conditions are used to model and verify ISIP/DFIT conditions.

In that context, the measured BHP pressure is applied directly to the perforation pipe. Fig. 2-7 shows that in that case the pressure is prescribed at the nodes at the intersections between perforation pipes and well pipe. Using predefined pressure conditions, the user should disable the connection between the perforations by reducing the well pipe conductivity to a small value.

2.6 Proppant transport analysis

The implementation of proppant placement in the Dynardo Hydraulic Fracturing Simulator is mainly based on the book of Yew and Weng [12] and the Dissertations of Liu [13] and Ribeiro [14]. In all these publications the numerical treatment of proppant placement is derived in 2.5D for a discrete planar vertical fracture. In this paper the corresponding governing equations are extended to the three-dimensional homogenized continuum approach applied in the simulator.

According to [13] the mass conservation of proppant inside a fracture can be written as

$$\frac{\partial(c\,\rho_P\,w)}{\partial t} + \nabla\cdot\left(c\,\rho_p\,\boldsymbol{v_p}\,w\right) = 0, \qquad (2\text{-}20)$$

with

$$c = \frac{V_P}{V_s}, \qquad (2\text{-}21)$$

where w is the fracture width, ρ_p is the apparent mass density of a single proppant, $\boldsymbol{v_p}$ is the proppant velocity, c.f. section 2.6.3, c is the proppant volume concentration, V_P is the proppant volume and V_S is the volume of slurry. In this context slurry is defined as the mixture of proppant and fluid

$$V_s = V_P + V_F, \qquad (2\text{-}22)$$

where V_F is the fluid volume. The corresponding slurry mass m_s can be written as

$$m_s = \rho_s V_s = \rho_P V_P + \rho_F V_F, \qquad (2\text{-}23)$$

where ρ_S is the slurry mass density and ρ_F is the fluid mass density. Assuming nonzero and constant apparent proppant mass density, Equation (2-20) can be rewritten as a differential volume balance equation

$$\frac{\partial(c\,w)}{\partial t} + \nabla\cdot\left(c\,\boldsymbol{v_p}\,w\right) = 0. \qquad (2\text{-}24)$$

The solution of Equation (2-24) requires the definition of boundary and initial conditions. No outflow of proppant is allowed over the fracture surface Γ_F

$$\left[\nabla\cdot\left(c\,\boldsymbol{v_p}\,w\right)\right]\cdot\boldsymbol{n} = 0 \;\; on\;\Gamma_F, \qquad (2\text{-}25)$$

where $\boldsymbol{n}$ is the vector normal to the fracture boundary. The inflow of proppant is defined as prescribed concentrations at the perforations Γ_P

$$c = c_P \;\; on\;\Gamma_P. \qquad (2\text{-}26)$$

At the beginning of the simulation zero proppant concentration is assumed for the entire model

$$c_{ini} = 0. \qquad (2\text{-}27)$$

By integrating Equation (2-24) over the fracture surface area S_F, represented in the local x-y-coordinate system, the integral volume balance equation is obtained

$$\iint_{S_F} \left[\frac{\partial(c\,w)}{\partial t} + \nabla\cdot\left(c\,\boldsymbol{v_p}\,w\right)\right] dx\,dy = 0. \qquad (2\text{-}28)$$

In the following this equation is extended to the homogenized continuum approach applied in this paper. In contrast to the discrete approach, the continuum model does not explicitly resolve the fracture geometry, but represents the fracture in terms of failure surfaces within the context of the material model, cf. sections 2.1 and 2.4. As a consequence, the fracture width is not directly available as a result of the mechanical analysis. The applied plasticity model represents the opening of a fracture (joint) in terms of plastic strains. In this context, it is to be noted that the applied multi-surface plasticity approach allows an unambiguous assignment of plastic strains to a particular joint set. Assuming, at first, a single joint set aligned with the x-y-plane (z-axis is normal to the joint set), the fracture opening can be written as

$$w = \int_z \varepsilon_N^{pl}\,dz, \qquad (2\text{-}29)$$

where ε_N^{pl} is the normal plastic joint strain. Substituting Equation (2-29) into Equation (2-28) yields

$$\iiint_V \left[\frac{\partial(c\,\varepsilon_N^{pl})}{\partial t} + \nabla\cdot\left(c\,\boldsymbol{v_p}\,\varepsilon_N^{pl}\right)\right] dx\,dy\,dz = 0. \qquad (2\text{-}30)$$

Since the balance must be satisfied independent of the (control) volume, the differential form of the balance equation for a homogenized fracture can be obtained

$$\frac{\partial(c\,\varepsilon_N^{pl})}{\partial t} + \nabla\cdot\left(c\,\boldsymbol{v_p}\,\varepsilon_N^{pl}\right) = 0. \qquad (2\text{-}31)$$

2.6.1 Finite element approximation

Equation (2-31), together with appropriate boundary and initial conditions, is solved by using the finite element method. As for example shown in [15], the standard Galerkin discretization, which is applied in the simulator, results in spurious oscillations. In order to stabilize the problem an artificial isotropic diffusivity is introduced. By extending Equation (2-31) with a corresponding diffusive term, the stabilized form of the balance equation is obtained

$$\frac{\partial(c\,\varepsilon_N^{pl})}{\partial t} + \nabla\cdot\left(c\,\boldsymbol{v_p}\,\varepsilon_N^{pl}\right) - \nabla\cdot(k_a\boldsymbol{I}\nabla c) = 0, \qquad (2\text{-}32)$$

where $\boldsymbol{I}$ is the identity matrix, and k_a is the artificial diffusion. Furthermore, the no outflow boundary condition given by Equation (2-25) is redefined as

$$\left[\nabla\cdot\left(c\,\boldsymbol{v_p}\,\varepsilon_N^{pl}\right) - \nabla\cdot(k_a\boldsymbol{I}\nabla c)\right]\cdot\boldsymbol{n} = 0. \qquad (2\text{-}33)$$

According to [15], Equation (2-32) is stable if the Peclet number is less than or equal to 2

$$PE = \frac{\varepsilon_N^{pl}\|\boldsymbol{v_p}\|\,l_{eq}}{k_a} \leq 2 \qquad (2\text{-}34)$$

where l_{eq} represents in the context of finite elements the mesh size. Consequently, Equation (2-32) is stable if

$$k_a \geq \frac{\varepsilon_N^{pl}\|\boldsymbol{v_p}\|\,l_{eq}}{2}. \qquad (2\text{-}35)$$

It is to be noted, that in the implementation the lowest possible diffusivity is calculated and applied separately for each element by defining the equivalent element size as

$$l_{eq} = \sqrt[3]{V_{e,prop}}, \tag{2-36}$$

where $V_{e,prop}$ is the proppant transport element volume.

2.6.2 Handling of multiple joint sets

Equation (2-31) represents the volume balance for a single fracture. The homogenized continuum approach in the simulator allows up to 7 joint sets (4 natural joint sets + 3 additional joint set due to intact failure) building a fracture network. In this paper, it is assumed that the concentration c represents the proppant concentration in the fracture network. Consequently, the proppant concentration is identical for all fractures. Furthermore it is assumed that the fracture specific parameters in Equation (2-31) can be superimposed

$$\varepsilon_N^{pl} = \sum_{j=1}^{n_J} \varepsilon_{N,j}^{pl}, \tag{2-37}$$

$$\boldsymbol{v_p}\, \varepsilon_N^{pl} = \sum_{j=1}^{n_J} \boldsymbol{v_{p,j}}\, \varepsilon_{N,j}^{pl}, \tag{2-38}$$

where n_j is the number of joint sets, $\varepsilon_{N,j}^{pl}$ is the plastic joint strain, $\boldsymbol{v_{p,j}}$ is the proppant transport velocity of joint set j. By substituting Equations (2-37) and (2-38) into Equation (2-31) and by applying the product rule and the sum rule to the time derivative, the volume balance equation for the homogenized fracture network can be written as

$$\frac{\partial c}{\partial t}\sum_{j=1}^{n_J} \varepsilon_{N,j}^{pl} + c\sum_{j=1}^{n_J} \frac{\partial \varepsilon_{N,j}^{pl}}{\partial t} + \nabla \cdot \left(c \sum_{j=1}^{n_J} \boldsymbol{v_{p,j}}\, \varepsilon_{N,j}^{pl} \right) = 0. \tag{2-39}$$

2.6.3 Proppant transport velocity

Because of the density contrast between proppant and fluid and because of other influences such as wall effects or bridging effects, the proppant travels with a different velocity than the slurry. According to [13] and [14] the proppant velocity $\boldsymbol{v_{P,J}}$ is expressed in terms of the slurry velocity $\boldsymbol{v_{S,J}}$, the settling velocity v_{Set} and retardation factors $k_{ret,J}$ and $f_{...}$. In this paper the following relationship is applied

$$\begin{pmatrix} v_{P,J,x} \\ v_{P,J,y} \\ v_{p,J,z} \end{pmatrix} = f_{Block,J}\, f_{\beta,J} \begin{pmatrix} k_{ret,J} v_{S,J,x} \\ k_{ret,J} v_{S,J,y} \\ f_{w,J} f_c [v_{S,J,z} - f_{freeze,J} v_{Set}] \end{pmatrix}. \tag{2-40}$$

The slurry velocity is obtained from the hydraulic model. As shown in section 2.5 slurry flow is described by the Darcy's law. Because of the superposition of the individual hydraulic conductivities the Darcy flux $\boldsymbol{q_{S,J}}$ in joint set J can be derived by using Equations (2-13) (2-16) and (2-17)

$$\boldsymbol{q_{S,J}} = -\boldsymbol{K_J} \nabla h\,. \tag{2-41}$$

The Darcy velocity, which corresponds to slurry velocity, is related to the Darcy flux by the porosity [16]. Within the homogenized continuum approach the porosity equates to the normal plastic joint strain. Consequently, the joint slurry velocity can be written as

$$\boldsymbol{v_{s,J}} = \frac{1}{\varepsilon_{N,j}^{pl}} \boldsymbol{q_{s,J}} = -\frac{1}{\varepsilon_{N,j}^{pl}} \boldsymbol{K_J} \nabla h \,. \qquad (2\text{-}42)$$

According to [17], [13] and [14] the settling of proppant can be calculated with modified Stokes's law

$$v_{Set} = f_{Re} v_{Stokes}, \qquad (2\text{-}43)$$

where v_{Stokes} is the Stoke's velocity and f_{Re} is a correction factor taking into account inertia effects. The Stokes velocity is defined as

$$v_{Stokes} = \frac{(\rho_P - \rho_F)\, g\, d_p^2}{18\, \mu_{F,Set}}, \qquad (2\text{-}44)$$

where ρ_P is the apparent proppant density, ρ_F is the fluid density, g is the standard gravity, d_P is the average proppant diameter and $\mu_{F,Set}$ is the dynamic fluid viscosity. It is to be noted that in the applied continuum approach the dynamic fluid viscosity used for the settling calculation, Equation (2-44) is generally different from the dynamic viscosity applied in the hydraulic model, cf. Equation (2-16). The settling velocity describes the relative movement of proppant with respect to the fluid. Therefore, the "real" dynamic fluid viscosity can be used in Equation (2-44). In contrast to that, the Darcy flow in the hydraulic model represents the movement of the slurry with respect to the rock mass. The slurry flow in a joint is greatly influenced by boundary effects which are not explicitly resolved in the continuum model. In order to match measured Bottom Hole Pressure histories a calibrated average fluid viscosity, taking into account those boundary effects in a homogenized manner, has to be applied in the hydraulic model. This calibrated viscosity is generally smaller than the actual dynamic fluid viscosity.

According to [17], Stoke's law is valid for particle Reynolds numbers less than 2. In this context the particle Reynolds number is defined as

$$Re_P = \frac{v_{Stokes}\, d_P\, \rho_F}{\mu_{F,Set}}. \qquad (2\text{-}45)$$

Fig. 2-8 shows for different fluid viscosities, the Stoke's settling velocity and the corresponding particle Reynolds numbers as functions of the Particle diameter. For fluids with low viscosity, e.g. slickwater, the limit of 2 is already exceeded for small proppant diameters.

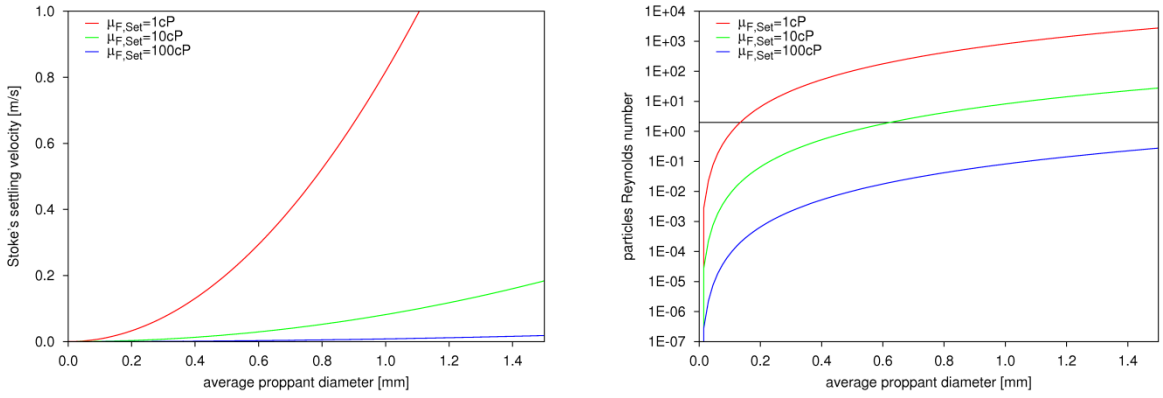

Fig. 2-8 Stoke's settling velocity and corresponding particle Reynolds numbers ($\rho_F = 1000\, kg/m^3$ and $\rho_P = 2500\, kg/m^3$)

For higher Reynolds numbers the Stoke's velocity needs to be corrected to account for inertia effects. In [14] an empirical, unit system dependent, correction factor is proposed. Assuming SI-units

(densities in kg/m^3, proppant diameter in m, fluid viscosity in $Pa \cdot s$ and standard gravity in m/s^2) the correction factor reads

$$f_{Re,SI} = 14.24 \frac{\mu_{F,Set}^{0.57}}{\rho_F^{0.29}(\rho_P - \rho_F)^{0.29} d_p^{0.86} g}. \tag{2-46}$$

If the parameters are defined in US units (densities in $slugs/ft^3$, proppant diameter in ft, fluid viscosity in psf s and standard gravity in ft/s²) the correction factor is given by

$$f_{Re,US} = 31.48 \frac{\mu_{F,Set}^{0.57}}{\rho_F^{0.29}(\rho_P - \rho_F)^{0.29} d_p^{0.86} g}. \tag{2-47}$$

Fig. 2-9 illustrates for a 1cP and 10cP fluid the influence of the correction factor on the settling velocity. For small proppant sizes, the settling velocity is slightly increased. With increasing proppant diameter the inertia effect becomes dominant and the settling velocity is significantly reduced.

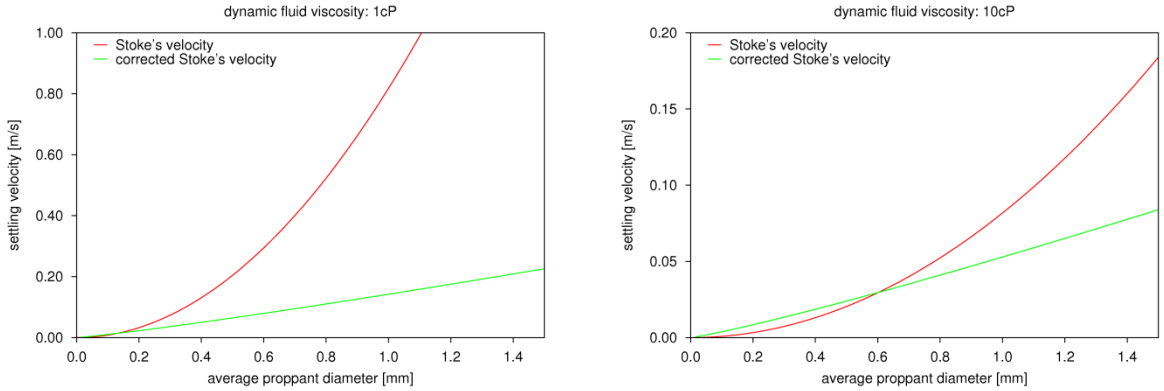

Fig. 2-9 Comparison between Stoke's and corrected Stoke's settling velocity for 1cP and 10cP fluid ($\rho_F = 1000\ kg/m^3$ and $\rho_P = 2500\ kg/m^3$)

In addition to the inertia effects the settling velocity is influenced by the proppant concentration in the fracture and by the fracture walls. According to [14] these effects can be taken into account by following retardation functions

$$f_{w,J} = 1 - 1.563\left(\frac{d_P}{w_J}\right) + 0.563\left(\frac{d_P}{w_J}\right)^2, \tag{2-48}$$

$$f_c = 1 - 3.12\left(\frac{c}{c_{crit}}\right) + 3.72\left(\frac{c}{c_{crit}}\right)^2 + 1.62\left(\frac{c}{c_{crit}}\right)^3 \geq 0, \tag{2-49}$$

where w_J is the fracture opening, as defined by Equation (2-60), and c_{crit} is the critical proppant concentration. It is to be noted that in [14] Equation (2-49) was originally defined for a critical proppant concentration of 0.65. In this paper the formula was reformulated allowing for arbitrary critical proppant concentrations. Fig. 2-10 shows plots of the two retardation functions. The settling velocity is reduced with increasing proppant concentration and decreasing fracture opening. In the presented approach, both scaling functions are additionally applied to the vertical component of the slurry velocity.

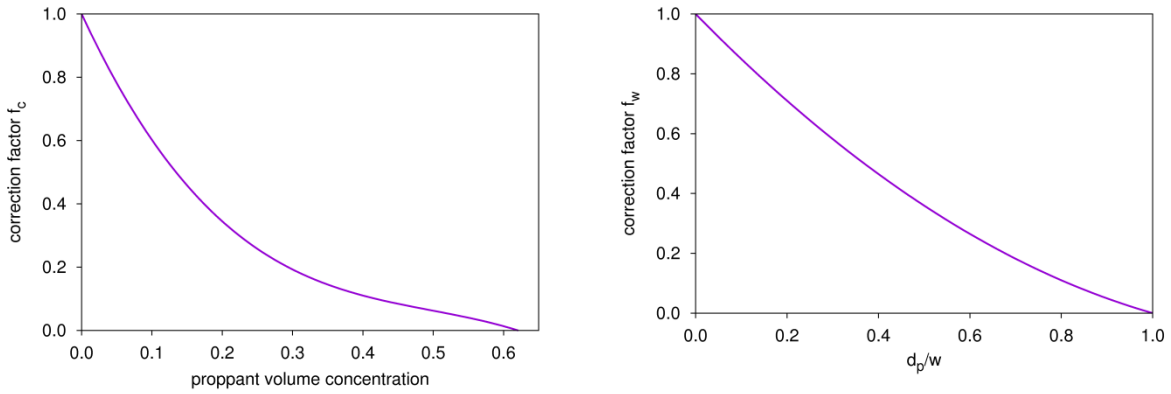

Fig. 2-10 Settling velocity retardation functions accounting for proppant concentration (left) and wall effects (right)

The horizontal proppant transport velocity is also influenced by the proppant concentration in the fracture and by effects of the fracture wall. Both effects are taken into account in the horizontal retardation factor $k_{ret,J}$. Based on the ideas and formulas given in [13] and [14], the following relationship is proposed

$$k_{ret,J} = 1 + \frac{d_P}{w_{c,J}} - 2.02\left[\frac{d_P}{w_{c,J}}\right]^2 \geq 0, \tag{2-50}$$

with

$$\left[\frac{d_P}{w_{c,J}}\right]^2 = \left[\frac{d_P}{w_J}\right]^2 + \left[1 - \frac{d_P^2}{w_J^2}\right]\left[\frac{c}{c_{crit}}\right]^{0.8} \tag{2-51}$$

where $w_{c,J}$ is an effective fracture width accounting for the interaction between proppant particles.

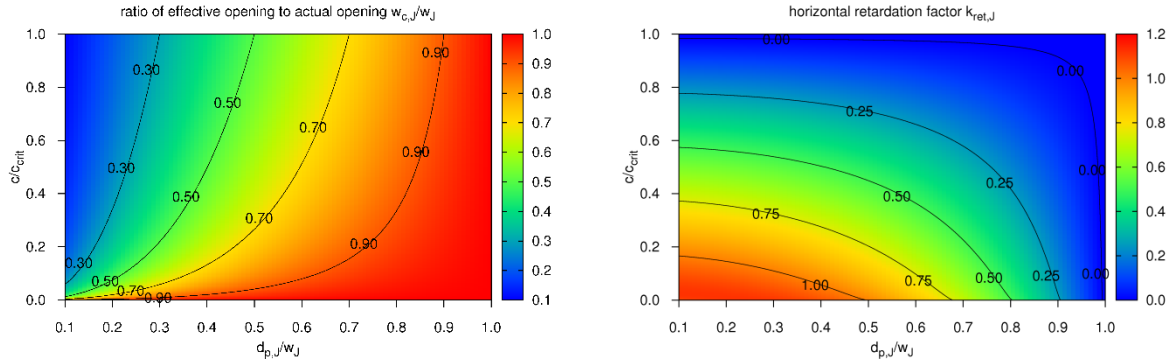

Fig. 2-11 ratio of effective fracture opening to actual fracture opening (left) and horizontal retardation factor (right)

Fig. 2-11 (left) illustrates the effect of the proppant concentration on the effective fracture opening. If the proppant concentration is zero, then the effective fracture opening is equal to the actual fracture opening. Increasing proppant concentrations result in effective fracture openings smaller than the actual fracture openings. Fig. 2-11 (right) shows a plot of the horizontal retardation factor as function of the proppant concentration and the fracture opening. On the one hand, the retardation factor approaches zero in narrow fractures, where the fracture opening is close to the proppant size, or in proppant-filled fractures, in which the concentration is close to the critical concentration. Consequently the proppant transport stops in those fractures. On the other hand the retardation factor might become greater than 1.0 for wide open fractures and low proppant concentrations. In that case the proppant particles travel faster than the fluid.

According to [18] and [19] the effect of proppant bridging, which prevents the particle flow in regions where the fracture width is several times the proppant diameter, has to be taken into account additionally by introducing a so-called blocking function. In the following it is assumed that proppant bridging occurs if the fracture aperture is less than three times the proppant diameter. In order to avoid discontinuities in the proppant flow, it is furthermore assumed that the proppant bridging effect vanishes if the fracture width becomes larger than four times the proppant size. Shiozawa and McClure [18] define the blocking function as a piece-wise linear function

$$f_{Block,J} = \begin{cases} 0 & w_J < 3d_P \\ \dfrac{w_J - 3d_P}{d_P} & 3d_P \le w_J \le 4d_P. \\ 1 & w_J > 4d_P \end{cases} \qquad (2\text{-}52)$$

Dontsov and Peirce [19] propose a smooth blocking function

$$f_{Block,J} = \begin{cases} 0 & w_J < 3d_P \\ \dfrac{1}{2}\left[1 - \cos\left(\pi \dfrac{3d_P - w_J}{d_P}\right)\right] & 3d_P \le w_J \le 4d_P. \\ 1 & w_J > 4d_P \end{cases} \qquad (2\text{-}53)$$

Both functions are implemented in the Dynardo simulator. In addition the effect of proppant bridging can be disabled. In the latter case the bridging function is set to 1. Fig. 2-12 (left) shows a plot of all three blocking functions which are available in the Dynardo simulator.

In the literature experimental investigations as well as numerical simulations of proppant transport are generally performed for vertical fractures. Therefore, the scaling functions presented above were originally developed to describe the relationship between slurry velocity and proppant transport velocity in vertical fractures. The Dynardo simulator is not limited to vertical fractures and the influence of the fracture inclination on the proppant transport velocity has to be taken into account. Because of the lack of experimental data, it is assumed that the proppant transport becomes more difficult or almost impossible if the joint orientation becomes horizontal. In this context, the following scaling function allowing the continuous reduction of the proppant transport velocity in non-vertical fractures is proposed

$$f_{\beta,J} = f_{\beta,0} + \frac{1 - f_{\beta,0}}{2}\left[\sin(2\beta_J - 90) + 1\right], \qquad (2\text{-}54)$$

where β_J is the joint dip ($0° \le \beta_J \le 90°$) and $f_{\beta,0}$ is the reduction factor in an horizontal fracture. Fig. 2-12 (right) shows a plot of this function for $f_{\beta,0} = 0$. The scaling factor is equal to 1 in a vertical fracture and reduces to 0 in a horizontal fracture. In that case proppant cannot be transported in bedding planes. It is to be noted that the influence of the joint dip can be removed by setting $f_{\beta,0} = 1$.

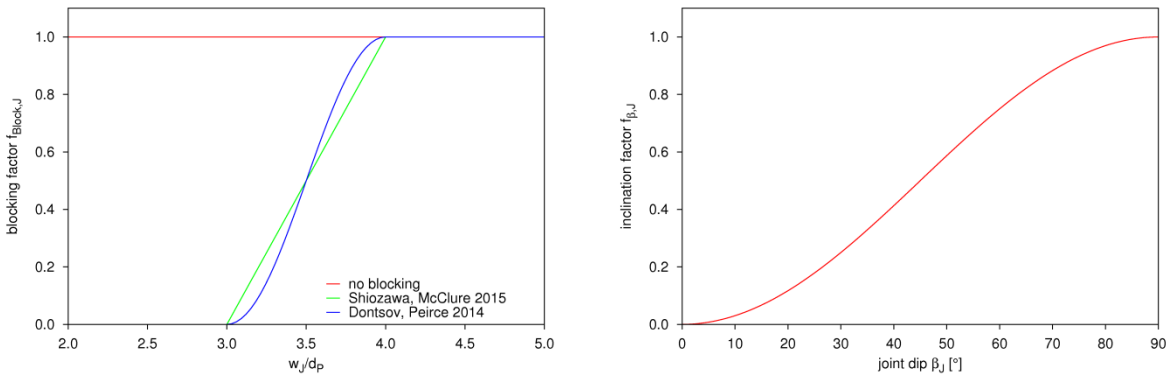

Fig. 2-12 blocking functions (left) and joint inclination function (right)

Finally, another optional scaling function is introduced to limit the proppant settling, especially after shut-in

$$f_{freeze,J} = \begin{cases} \dfrac{\|\boldsymbol{v}_{S,J}\|}{v_{Set}} & 0 \le \|\boldsymbol{v}_{S,J}\| \le v_{Set} \\ 1 & \|\boldsymbol{v}_{S,J}\| > v_{Set} \end{cases}, \qquad (2\text{-}55)$$

where $\boldsymbol{v}_{S,J}$ is the slurry velocity, given by Equation (2-42), and v_{Set} is the settling velocity defined in Equation (2-43). By using this function the settling velocity cannot be greater than the fluid velocity. This approach allows to "freeze" the proppant distribution after the pumps have stopped.

2.6.4 Handling of multiple proppant classes

According to [20], the traditional fracture treatment starts with smaller particle size proppant and tailors with larger particle size proppant to maximize the near wellbore conductivity. In order to represent such a proppant pumping schedule, the Dynardo simulator allows the definition of multiple proppant classes. In this context, a particular proppant class is represented by the corresponding proppant inflow, average particle diameter and apparent density. The numerical treatment is based on the assumption of superposition of the individual proppant classes. The proppant transport simulation is performed for each class separately. In each time step, the update of the proppant concentration starts with class with the largest average particle diameter and is successively followed by the classes with smaller particles. The individual proppant transport models are weakly coupled. In the evaluation of the proppant velocity, cf. section 2.6.3, the total proppant concentration, defined as the sum of the individual proppant class concentrations, is used. The total proppant concentration is additionally applied in the coupling to the hydraulic model, cf. section 2.7.

2.6.5 Proppant model adaptation

Proppant transport is only possible in fractures but not in intact rock. Therefore, the proppant transport simulation can be performed on a reduced finite element model. Only the fractured elements need to be resolved in this model. As a result the number of unknowns in the proppant transport model is significantly smaller compared to the mechanical and hydraulic model. Since the fractured elements are not known in advance, an adaptive solution procedure has to be applied.

In order to simplify the transfer of variables the proppant transport finite element model is identical to the hydraulic model. At the beginning of the simulation a base proppant transport model is generated based on the initial hydraulic model. It is to be noted that this base model represents the full reservoir model. The mesh adaptation is performed at the beginning of each time step. In a first step the fracture parameters (coupling with the mechanical model) and the hydraulic heads (coupling with the hydraulic

model), are updated in the base proppant model. In a second step all non-fractured elements, except for the perforations, are deleted and the reduced model is generated. In a last step, the proppant concentrations obtained at the end of the previous time step are defined as initial conditions in the reduced model. In this context, all nodes, which were not considered in the previous time step, are initialized to zero. Finally, the proppant transport simulation is performed and the proppant concentrations are updated on the reduced model.

2.6.6 Proppant transport post-processing

The Dynardo simulator allows the post-processing of the proppant concentrations of the individual proppant classes as well as the total proppant concentrations. Furthermore, the proppant transport velocity and the proppant mass per fracture area can be post-processed. In this context, the proppant mass in a joint is given by

$$m_{P,J} = \rho_P \, c \, V_J, \tag{2-56}$$

where c is the total proppant concentration. The joint volume V_J is calculated as

$$V_J = \varepsilon_{N,J}^{pl} \, V_e, \tag{2-57}$$

where V_e is the element volume. For the sake of simplicity, it is assumed that the joint surface area is given by

$$A_{SF,J} = l_{eq}^2, \tag{2-58}$$

where l_{eq} is the equivalent element length given by Equation (2-36). By substituting Equation (2-57) into Equation (2-56) and by using Equations (2-36) and (2-58), the proppant mass per fracture area can be expressed as

$$\frac{m_{P,J}}{A_{SF,J}} = \frac{\rho_P \, c \, \varepsilon_{N,J}^{pl} \, V_e}{l_{eq}^2} = \rho_P \, c \, \varepsilon_{N,J}^{pl} \, l_{eq}. \tag{2-59}$$

In addition to the above data, which are only available at pre-defined post-processing points, the proppant inflow, the proppant concentration at perforation and the proppant volume balance can be monitored in every time step during the simulation.

2.7 Permeability update - mechanical and proppant-transport to hydraulic coupling

According to [5], the joint set permeability (hydraulic model) is related to the joint opening (mechanical model). If a joint opens up, then the permeability increases. If, in addition, proppant is pumped, then the permeability of a fracture in which proppant is placed reduces compared to a fracture with identical opening but without proppant. Consequently, the proppant concentration (proppant transport model) has also an effect on the joint permeability. The Dynardo simulator accounts for both effects. As a result, the hydraulic model is coupled to the mechanical model as well as the proppant transport model.

In the mechanical analysis, the development of fractures is represented by a plastic material model. As a result, the joint set opening is not directly measured but needs to be calculated based on the plastic strains. Additional history variables are introduced which monitor the normal plastic strains of every joint set during the mechanical analysis. Both failure modes, tensile and shear, result in a normal plastic strain component. The amount of normal plastic strain due to shear failure can be controlled by the dilatancy angle. For a specific joint set, the normal plastic strain increases only if the

corresponding yield surfaces are active. The total mechanical (geometrical) joint opening E_J of joint set J is defined as:

$$E_J = \varepsilon_{N,J}^{Pl} S_J \tag{2-60}$$

where $\varepsilon_{N,J}^{Pl}$ is the normal plastic joint strain and S_J is the average activated joint set distance. The activated joint set distance is an input parameter and needs to be calibrated. In order that the continuum theory remains valid, the activated joint set distance is limited by an equivalent element length l_{eq}:

$$S \leq l_{eq}. \tag{2-61}$$

The equivalent element length is a one-dimensional measure for the size of the domain represented by an integration (material) point. According to Reference [21], the equivalent element length l_{eq} for an 8-node brick element with 8 integration points can be defined as:

$$l_{eq} = \sqrt[3]{\frac{V_{e,mech}}{8}} \tag{2-62}$$

where $V_{e,mech}$ is the element volume. In this context, it is to be noted that the hydraulic and proppant transport analysis is performed on a refined mesh. Each mechanical element is replaced by 8 hydraulic or proppant transport elements. Therefore, the equivalent element length, defined in Equation (2-62) is identical to the length given by Equation (2-36), in which the proppant transport element volume is applied.

The consideration of proppant in the update of hydraulic joint permeability is based on ideas given in [18]. The total mechanical opening, given by Equation (2-60), is decomposed as

$$E_J = E_{J,o} + E_{J,p} \tag{2-63}$$

where $E_{J,p}$ is the equivalent proppant bed thickness and $E_{J,o}$ is the remaining opening without proppant. The equivalent proppant bed thickness is a theoretical measure which represents the volume of slurry with critical proppant concentration in the fracture. It is to be noted that this measure does not depend on the proppant diameter and as a consequence value might be smaller than the proppant diameter. The equivalent proppant bed thickness is defined as

$$E_{J,p} = \frac{c}{c_{crit}} E_J, \tag{2-64}$$

where c is the total proppant concentration and c_{crit} is the critical proppant concentration.

Furthermore, it is assumed that the total joint permeability k_J can decomposed as

$$k_J = k_{J,o}(E_{J,o}, \sigma_{N,J}) + k_{J,p}(E_{J,p}, \sigma_{N,J}), \tag{2-65}$$

where $\sigma_{N,J}$ is the normal joint stress, $k_{J,0}$ is the permeability of a joint without proppant, cf. section 2.7.1, and $k_{J,p}$ is the proppant bed permeability, cf. section 2.7.2.

2.7.1 Permeability in joint without proppant

In the original derivation of the joint set permeability in Reference [5], a laminar flow between two smooth planes is assumed. In reality, the joint surface is neither planar nor smooth. Consequently, the mechanical opening must be related to the effective hydraulic opening of the idealized joint set [22] [23]. In the simulator, the following relationship is applied:

$$e_J = \frac{E_{J,o}}{r_{Ee}}, \qquad (2\text{-}66)$$

where e_J is the effective hydraulic opening and r_{Ee} is a prescribed ratio between both opening measures. In most applications of the simulator, a ratio between 1 and 2 is used initially, and later adjusted and verified during the calibration process.

The relationship between the effective hydraulic opening and the hydraulic joint set permeability is given by a cubic law:

$$k_{J0} = \frac{e_J^3}{12\, S_J\, R_{C,J}}, \qquad (2\text{-}67)$$

where $R_{C,J}$ is the joint roughness coefficient. This relationship is visualized in Fig. 2-13. In order to be able to limit the flow in the joint set, a maximum effective hydraulic opening e_{max} is introduced. This maximum hydraulic opening results in the maximum hydraulic conductivity, and is related to the in-situ stress, the fluid, and the proppant placement condition. A limitation to this value can usually be seen in experimental data. This parameter is one of the most important model parameters that should be properly calibrated.

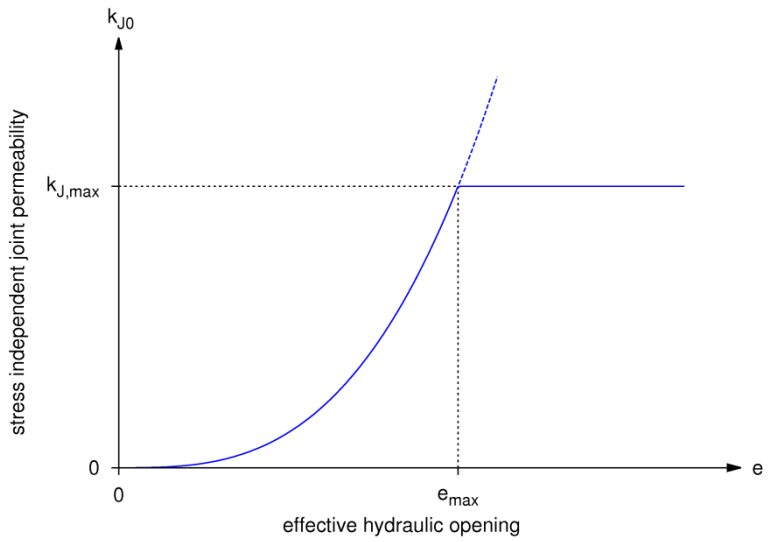

Fig. 2-13 Coupling between joint set permeability and joint set opening

Since the joint opening is described by a plasticity model, the closure of joints, i.e., the reduction of normal plastic joint strains, is not represented in the mechanical model. The effect of compressive normal joint stresses on the joint set permeability is not taken directly into account in Eq. (2-67). As shown in Reference [23], this effect can be observed in experiments and will have a significant influence on the resulting joint conductivity during production. The simulator optionally allows for this effect to be managed. If the stress dependency is enabled, then the joint set permeability is calculated as:

$$k_{J,o}(e_J, \sigma_{N,J}) = f(\sigma_{N,J}) k_{J0}(e_J), \qquad (2\text{-}68)$$

where k_{J0} is the stress independent joint set permeability given by Eq. (2-67), f is a dimensionless scaling factor ranging from a minimum value to 1, and $\sigma_{N,J}$ is the normal joint stress. Based on [24] the following stress dependency function is implemented:

$$f(\sigma_{N,J}) = \begin{cases} 1 & \sigma_{N,J} > 0 \\ (1 - f_{min})\left[1 - \left(\frac{\sigma_N}{D}\right)^{\frac{1}{n}}\right]^3 + f_{min} & D \leq \sigma_{N,J} \leq 0, \\ f_{min} & \sigma_{N,J} < D \end{cases} \quad (2\text{-}69)$$

where D is the limit compressive stress (negative), f_{min} is the minimum scaling factor, and n is a shape factor. Fig. 2-14 visualizes the influence of that shape factor. For the post-processing of the joint openings, the openings are recalculated by introducing the stress dependent joint set permeability into the cubic law, Eq. (2-67).

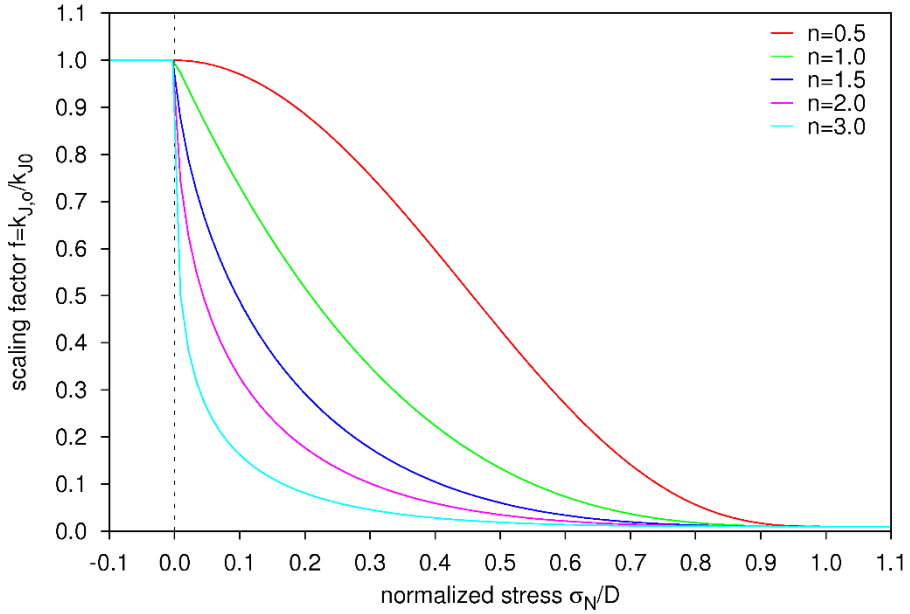

Fig. 2-14 influence of the shape factor on stress dependency of the joint permeability (f_{min}=0.01)

The conductivity decline function (stress dependency function) is additionally influenced by the proppant placement in the fractures. In general, higher pressures are required to close a fracture which is filled with proppant than a fracture without proppant. If in the simulation proppant transport is explicitly simulated, then the influence of proppant is directly considered in the proppant bed permeability, cf. section 2.7.2. Otherwise, this effect is taken into account in a simplified way by defining two different stress dependency functions, namely limit stress and minimum scaling factor. The stress dependency function for joints with proppant is applied in all elements having proppant-accepting mechanical joint openings and which are connected to perforation clusters with elements having all proppant-accepting joint openings, cf. Section 2.9.1. In all other elements, the stress dependency function for joints without proppant is used. Usually the stress dependency parameters are derived from lab tests of conductivity at varying proppant concentrations and normal stress conditions.

2.7.2 Proppant bed permeability

The permeability of a proppant filled fracture, which means that the critical proppant concentration is reached in that particular fracture, depends on the permeability of the proppant particle itself and on the proppant bed porosity. Normally the average permeability of the proppant pack is experimentally obtained by using long term conductivity tests according to ISO 13503-5, cf. [25]. Typically such a test is performed at constant temperature for a proppant loading of 2 lb/ft² and very low water velocities. Furthermore, a constant closure pressure is applied to the fracture surface and the measurement is performed over 50 hours. Many manufacturers of proppants already provide for their

products either the proppant pack permeability or the proppant pack conductivity as function of the normal stress acting on the fracture. In this context the proppant pack permeability $\bar{k}_p$ is related to the proppant pack conductivity $\bar{c}_p$ by the proppant pack width w_p

$$\bar{c}_p = w_p \bar{k}_p. \tag{2-70}$$

In the Dynardo simulator the experimentally obtained relationship between closure pressure and proppant pack permeability can be directly used to define the permeability of the equivalent proppant bed. The user provides in an ASCII input file the corresponding relationship.

In contrast to the experiments, which represent the flow in the fracture itself (the cross-section area to flow is equal to the cross-section area of the fracture), the finite elements in the Dynardo simulator describe in a homogenized way the flow in the jointed rock, where the proppant bed is embedded in the intact rock. Therefore, the proppant bed permeability is averaged as

$$k_{J,p}(E_{J,p}, \sigma_{N,J}) = \bar{k}_p(\sigma_{N,J}) \frac{E_{J,p}}{S_J}, \tag{2-71}$$

where $\bar{k}_p$, is the experimental proppant pack permeability, $\sigma_{N,J}$ is the closure pressure, $E_{J,p}$ is the actual equivalent proppant bed thickness, cf. Eq. (2-63), and S_J is the activated joint set distance.

2.7.3 Influence of Intact Failure on Hydraulic Conductivity Tensor

In addition to joint failure, the intact rock might fail as well, and the hydraulic conductivity of the jointed rock increases. In order to capture this phenomenon, up to three additional joint sets, one for tensile failure and two for shear failure, are introduced in case of intact rock failure. These additional joint sets are introduced if the corresponding intact rock failure criterion is violated for the first time. In the case of tensile failure where the Rankine yield surface becomes active, the additional joint is oriented perpendicular to the maximum principal stress direction. In the case of shear failure where the Mohr-Coulomb yield surface becomes active, the orientation of two additional joint sets coincides with the orientation of the shear failure planes in that step. After initialization of the additional joint sets, the orientation is fixed for that element for the duration of the simulation. For these additional joint sets, the mechanical-hydraulic coupling is performed in the same way as for the pre-defined joint sets.

From experience in shale reservoirs, the hydraulic conductivity change primarily from intact failure occurs in fracture barriers, which usually represents reservoir layers without vertical joint sets.

2.8 Flow force update - hydraulic-mechanical coupling

Fluid flow in joints results in normal forces and shear forces at the joint walls [5]. The flow forces are related to the pore-pressure gradient. In the global orientation, the flow force vector $\boldsymbol{J_{ff}}$ acting on the element volume (body force) can be written as:

$$\boldsymbol{J_{ff}} = \rho\, g\, \boldsymbol{I} \qquad \boldsymbol{I}^T = \left[\frac{\partial h}{\partial x} \quad \frac{\partial h}{\partial y} \quad \frac{\partial h}{\partial z}\right] \tag{2-72}$$

where ρ is the fluid density, g is the standard gravity, and $\boldsymbol{I}$ is the gradient of the hydraulic head. The corresponding nodal force vector is obtained by integration of the flow force vector over the element volume. The individual nodal contributions are assembled and transferred to the mechanical model. Because of the incremental solution procedure, only the variation in the flow forces is added to the nodal forces in the mechanical model at every time step.

2.9 Post Processing

In addition to the traditional ANSYS post-processing functionality, e.g., stress plots, the simulator provides additional hydraulic fracturing specific outputs. These additional post-processing features are provided as parameterized APDL macros or as predefined work-spaces in Tamino. In order to reduce the amount of data which is produced during the simulation and in order to reduce the total simulation time, the frequency of post-processing steps is also parameterized. The additional post-processing includes:

- bottom hole pressure and slurry rate over time (per perforation and per stage)
- fluid and fracture volume balance, e.g. fluid inflow and created joint volumes over time
- plots of joint set openings, joint set conductivities
- pore-pressure plots
- plots of the stimulated rock including microseismic events (all plastic elements, connected water-accepting plastic elements and connected proppant-accepting plastic elements) and the corresponding stimulated rock volume over time
- plastic activity over time
- connected drainage volume
- fracture extension compared to microseismic events
- proppant volume balances
- proppant concentration
- proppant mass per fracture area

In addition to this predefined post-processing macros, all results can be exported into ASCII files.

2.9.1 Calculation of Connected Water and Proppant-Accepting Volume

Based on the mechanical joint openings, elements are identified as water-accepting or as proppant-accepting. An element becomes water-accepting if the mechanical opening of at least one joint set exceeds a predefined threshold. This threshold is parameterized. Usually a threshold of 0.1 mm is applied. A proppant-accepting element is identified if the mechanical opening of at least one joint set exceeds a multiple of the average proppant size. The factor and the average proppant size are also parameters of the model. In most of the reservoirs, a threshold of 3 times the average proppant size is applied.

In addition to the water and proppant-accepting elements, the corresponding connected sets of water and proppant-accepting elements are identified. An element is part of the set of connected water-accepting elements if the fluid can flow from any perforation into that element only by flowing through the other elements in that set. The sets of connected water and of connected proppant-accepting elements are continuously updated during the simulation. At the beginning of the simulation, the perforation elements are added to the connected sets. After every mechanical step, the water and proppant-accepting elements are identified. Based on the connected sets from the previous step, the neighbouring water or proppant-accepting elements are selected and added to the corresponding connected set. Two elements are neighbours if they are connected by at least one node. This selection algorithm is continued until no new neighbour elements are found. The sets of connected elements are history dependent.

For connected proppant-accepting volumes, the possibility of successful proppant placement is presumed. If proppant is placed in the fractures, it has an influence on the conductivity decline function, cf. Section 2.7.1. The stress dependency function for joints with proppant is only used for elements which are part of the set of connected proppant-accepting volume. Otherwise the stress

dependency function for joints without proppant is applied even if the opening is larger than the proppant-accepting opening threshold.

2.9.2 Calculation Connected Drainage Volume

Based on the set of connected proppant-accepting elements, the drainage volume can be calculated. The drainage volume is defined by all elements which can be drained during the production time of the well from the set of connected proppant-accepting elements. The corresponding elements are identified by selecting, from the set of "connected proppant-accepting elements," all elements which satisfy the following criteria:

- The element is in the same element layer of the layered reservoir as the connected proppant-accepting element. This is based on the assumption that only the "horizontal" initial permeability of unstimulated rock provides a mechanism for flow through unstimulated rock, this horizontal permeability being several orders of magnitude larger than the effective vertical permeability.
- The distance between the element center and the center of the proppant-accepting element is less than the drainage radius.

References

[1] ANSYS, Inc., ANSYS ® , Release 14.5, Canonsburg, PA, 2013.

[2] Dynardo GmbH, multiPlas – elastoplastic material models for ANSYS, Version 5.0.593, Weimar, 2013.

[3] Dynardo GmbH, 3D Hydraulic fracturing simulator, version 3.7.4, documentation.ppt, Weimar, 2013.

[4] Dynardo GmbH, optiSLang ® - The optimizing Structural Language, Version 4.1.0, Weimar, 2013.

[5] W. Wittke, Felsmechanik: Grundlagen für wirtschaftliches Bauen im Fels, Springer-Verlag, 1984.

[6] J. Will, „Beitrag zur Standsicherheitsberechnung im geklüfteten Fels in der Kontinuums- und Diskontinuumsmechanik unter Verwendung impliziter und expliziter Berechnungsstrategien," in *Berichte des Institutes für Strukturmechanik 2/99*, Dissertation, Bauhaus Universität Weimar, 1999.

[7] L. Weijers, "Evaluation of Oil Industry Stimulation Practices for Engineered Geothermal Systems, Pinnacle Report DOE-PS36-04GO94001," October 2010.

[8] J. Will and R. Schlegel, "Simulation of hydraulic fracturing of jointed rock," in *Proceedings of European Conference on Fracture*, Dresden, 2010.

[9] J. C. Simo and T. J. Hughes, Computational Inelasticity, Springer, 1998.

[10] K. J. Bathe, Finite element procedures, Prentice Hall, 1985.

[11] M. Jirasek and Z. P. Bazant, Inelastic Analysis of Structures, John Wiley & Sons, 2001.

[12] C. H. Yew and X. Weng, Mechanics of Hydraulic Fracturing, Elsevier, 2015.

[13] Y. Liu, "Settling and hydrodynamic retardation of proppants in hydraulic fractures," Dissertation, University of Texas at Austin, 2006.

[14] L. H. N. Ribeiro, "Development of a three-dimensional compositional hydraulic fracturing simulator for energized fluids," Dissertation, University of Texas at Austin, 2013.

[15] D. Kuzmin, "A Guide to Numerical Methods for Transport Equations," University Erlangen-

Nuremberg, 2010. [Online]. Available: http://www.mathematik.uni-dortmund.de/~kuzmin/Transport.pdf. [Accessed 19. Januar 2017].

[16] H. M. Haitjema and M. P. Anderson, "Darcy Velocity Is Not a Velocity," *Groundwater,* vol. 54, no. 1, p. 1, 2016.

[17] P. B. Gadde, Y. Liu, J. Norman, R. Bonnecaze and M. M. Sharma, "Modeling Proppant Settling in Water-Fracs," in *SPE Annual Technical Conference and Exhibition*, Houston, Texas, 2004.

[18] S. Shiozawa and M. McClure, "Comparison of Pseudo-3D and Fully-3D Simulations of Proppant Transport in Hydraulic Fractures, Including Gravitational Settling, Formation of Proppant Banks, Tip-Screen Out, and Fracture Closure," in *SPE Hydraulic Fracturing Technology Conference*, The Woodlands, Texas, USA, 2016.

[19] E. V. Dontsov and A. P. Peirce , "Slurry flow, gravitational settling and a proppant transport model for hydraulic fractures," *Journal of Fluid Mechanics,* vol. 760, pp. 567-590, December 2014.

[20] F. Liang, M. Sayed, G. A. Al-Muntasheri, F. F. Chang and L. Li, "A comprehensive review on proppant technologies," *Petroleum,* vol. 2, no. 1, pp. 26-39, 2016.

[21] R. Pölling, Eine praxisnahe, schädigungsorientierte Materialbeschreibung von Stahlbeton für Strukturanalysen, Dissertation, Ruhr-Universität Bochum, 2000.

[22] N. Barton, S. Bandis and K. Bakhtar, "Strength, deformation and conductivity coupling of rock joints," *International Journal of Rock Mechanics and Mining Sciences & Geomechanics Abstracts,* vol. 22, no. 3, p. 121–140, June 1985.

[23] M. T. Z. Iragorre, Thermo-hydro-mechanical analysis of joints a theoretical and experimental study, Barcelona: Phd-Thesis, Univesitat politècnica de Catalunya, 2010.

[24] A. F. Gangi, "Variation of whole and fractured porous rock permeability with confining pressure," *International Journal of Rock Mechanics and Mining Sciences & Geomechanics Abstracts,* vol. 15, no. 5, pp. 249-257, 1978.

[25] J. Kullman, "The Complicated World of Proppant Selection," 2011. [Online]. Available: http://images.sdsmt.edu/learn/speakerpresentations/Kullman.pdf. [Accessed 9 März 2017].

[26] T. Most and J. Will, "Efficient sensitivity analysis for virtual prototyping," in *Proceedings of the 6th European Congress on Computational Methods in Applied Sciences and Engineering*, Vienna, 2012.